

Article

Hierarchical Porous and Three-Dimensional MXene/SiO₂ Hybrid Aerogel through a Sol-Gel Approach for Lithium–Sulfur Batteries

Jianping Zhou¹, Ziyuan Pei¹, Zhuyin Sui^{1,*}, Ying Liang², Xiufeng Xu¹, Yongpeng Li¹, Yulin Li¹, Jingyi Qiu^{3,*} and Qi Chen^{2,*} ¹ School of Chemistry & Chemical Engineering, Yantai University, Yantai 264005, China² State Key Laboratory of Marine Resource Utilization in South China Sea, Hainan Provincial Key Lab of Fine Chemistry, School of Chemical Engineering and Technology, Hainan University, Haikou 570228, China³ Research Institute of Chemical Defense, Beijing 100191, China

* Correspondence: suizy@ytu.edu.cn (Z.S.); qiujingyi1202@163.com (J.Q.); chenqi@hainanu.edu.cn (Q.C.)

Abstract: A unique porous material, namely, MXene/SiO₂ hybrid aerogel, with a high surface area, was prepared via sol-gel and freeze-drying methods. The hierarchical porous hybrid aerogel possesses a three-dimensional integrated network structure of SiO₂ cross-link with two-dimensional MXene; it is used not only as a scaffold to prepare sulfur-based cathode material, but also as an efficient functional separator to block the polysulfides shuttle. MXene/SiO₂ hybrid aerogel as sulfur carrier exhibits good electrochemical performance, such as high discharge capacities (1007 mAh g⁻¹ at 0.1 C) and stable cycling performance (823 mA h g⁻¹ over 200 cycles at 0.5 C). Furthermore, the battery assembled with hybrid aerogel-modified separator remains at 623 mA h g⁻¹ over 200 cycles at 0.5 C based on the conductive porous framework and abundant functional groups in hybrid aerogel. This work might provide further impetus to explore other applications of MXene-based composite aerogel.



Citation: Zhou, J.; Pei, Z.; Sui, Z.; Liang, Y.; Xu, X.; Li, Y.; Li, Y.; Qiu, J.; Chen, Q. Hierarchical Porous and Three-Dimensional MXene/SiO₂ Hybrid Aerogel through a Sol-Gel Approach for Lithium–Sulfur Batteries. *Molecules* **2022**, *27*, 7073. <https://doi.org/10.3390/molecules27207073>

Academic Editor: Chongjun Zhao

Received: 22 September 2022

Accepted: 19 October 2022

Published: 20 October 2022

Publisher's Note: MDPI stays neutral with regard to jurisdictional claims in published maps and institutional affiliations.



Copyright: © 2022 by the authors. Licensee MDPI, Basel, Switzerland. This article is an open access article distributed under the terms and conditions of the Creative Commons Attribution (CC BY) license (<https://creativecommons.org/licenses/by/4.0/>).

Keywords: MXene; SiO₂; hybrid aerogel; porous structure; lithium–sulfur battery

1. Introduction

With the development of electronic devices and electric vehicles, the demand for energy-efficient and cost-effective secondary batteries is growing, which has firmly drawn considerable attention and captured the heart of researchers [1]. Among energy storage applications, lithium–sulfur batteries (LSBs), as the next-generation inspiring devices, have shown the attractive potential by virtue of high energy density (up to 2600 Wh kg⁻¹), environmental benignancy, and reduced cost [2]. Although significant progress has been made, its large-scale implementation still faces many problems, in particular, mechanical degradation of the cathode because of the huge volume change (nearly 80%) in the process of discharging and charging, the inherent insulation property of sulfur, and the loss of active substances (resulting in shuttle effect of soluble polysulfides) [3,4]. The main obstacle behind the poor battery performance is the dissolution and “shuttle effect” of intermediate polysulfides, which begins with the battery discharge process [5,6].

In order to solve the above problems related to LSBs, progress has been made in various sulfur hosts to block the diffusion and shuttle of polysulfides, so as to obtain more efficient LSBs [7,8]. Different materials with abundant adsorption sites, such as conductive polymers [9,10], porous carbon nanofibers [11], hierarchical porous carbon [12], carbon nanotubes [13], and metal oxides [14,15], are designed to capture active materials to deal with polysulfide shuttle effect, improve battery discharge capacity, and enhance cycling stability. Previous studies have shown these methods can increase capacity and improve the cyclability, but there is still a large amount of loss of active substances. The main reason is that there is no strong adsorption potential, which can not only adsorb polar polysulfides but also solve the loss of active substances.

The continuous progress in research and development of functional separators has significantly improved the cycling performance of LSBs [16,17]. The functional separator is easy to prepare, and it can be used as an effective barrier to inhibit the shuttle effect of polar polysulfides across separators, and as a reservoir for different sulfur species [18,19]. Different types of modified separators, such as the dual-doped mesoporous carbon-modified separator [20], titanium dioxide-modified separator [21], and metal–organic framework-based separator [22], have been prepared to limit the movement of polysulfide intermediates to the cathode. The use of two-dimensional materials in functional separators of LSBs has aroused a great interest of researchers, owing to their large specific surface area and rich functional groups. For example, Huang's team prepared a permselective graphene oxide-modified separator, which allows lithium ions to penetrate, but repels anions. The resultant separator can adequately block the shuttle of polysulfides through steric exclusion and electrostatic repulsion, and the corresponding capacity loss rate of the battery with the modified separator was 0.23% per cycle [23]. To overcome the challenge of polysulfide diffusion, Cui and his colleagues prepared a bifunctional separator with two-dimensional black-phosphorus nanosheets, which can capture different polysulfides through the strong interaction and re-activation of captured polysulfides owing to its high lithium ion diffusivity and electron conductivity [24].

MXene obtained from MAX phase materials is a new kind of two-dimensional transition layered metal carbides/nitrides/carbonitrides [25,26]. MXene exhibits great potential in LSBs because of its rich surface functional groups and excellent conductivity, which play important roles in immobilizing soluble polysulfides [27,28]. However, because of hydrogen bonding interactions and van der Waals force, MXene sheets tend to restack, which will inevitably result in the loss of the active sites and limit the adsorption and catalytic conversion of polar polysulfides. Therefore, it is essential to alleviate the aggregation of MXenes and assemble MXenes into three-dimensional (3D) porous materials, so as to better promote the effective adsorption/conversion of polysulfides and improve the battery performance.

Recently, SiO₂ has been developed as a sulfur host material or functional separator for LSBs. For example, Kou et al. reported a flexible carbon/SiO₂ membrane material through a phase inversion method for LSBs. The as-designed carbon/SiO₂-derived sulfur-based cathodes presented long-term cycling stability [29]. Li et al. prepared a SiO₂ particle-modified polypropylene (PP) separator by immersing the PP membrane in the hydrolysis solution of tetraethyl orthosilicate (TEOS). The rate capability and cyclic stability of the LSBs using the SiO₂-modified separator were greatly improved [30]. However, the work on MXene/SiO₂-based aerogel materials for high-performance LSBs has never been reported.

Herein, we report a design of a unique porous material, namely, MXene/SiO₂ hybrid aerogel (MSHA) with a high specific surface area value (572 m² g⁻¹) via facile sol-gel and freeze-drying methods. The hierarchical porous hybrid aerogel can be used not only as a novel host for the sulfur-based cathode but also as an efficient functional separator to alleviate the shuttle effect of polysulfides. MSHA as a sulfur carrier exhibits high discharge capacities, excellent rate capability, and good cycling performance. MXene sheets can help to provide a conductive network for rapid electron transfer between the collector and active substances. It is worth noting that the SiO₂ components are used as pillars to support MXene sheets to construct open spaces. Furthermore, the battery containing MSHA-functionalized separator shows high capacities (623 mA h g⁻¹ over 200 cycles at 0.5 C). We believe that this work will provide further impetus for the researchers to explore applications of MXene-based composite aerogel in LSBs.

2. Results and Discussion

2.1. Preparation of MSHA

Figure 1 shows the preparation process of MSHA. It starts with the employment of aqueous Ti₃C₂T_x MXene solution as the precursor. MXene (Ti₃C₂T_x) sheets were prepared by selective removal of Al from Ti₃AlC₂ MAX material with a wet etching (HCl + LiF)

system [31]. Transmission electron microscopy analysis (Figure S1) illustrates the two-dimensional nature of MXene sheets. MXene sheets can be applied to prepare porous materials by assembling different materials through sol-gel and freeze-drying methods [32]. After TEOS was added into MXene aqueous dispersion, TEOS can be converted into SiO_2 by hydrolysis and polymerization reaction [33]. The hydroxyl functional groups on the surface of SiO_2 can form hydrogen bond with oxygenated functional groups of $\text{Ti}_3\text{C}_2\text{T}_x$ MXene. As the reaction proceeded, MXene/ SiO_2 hybrid hydrogel was obtained. The SiO_2 formed in situ is randomly mixed with MXene. In addition, in order to have a good understanding of the hybrid hydrogel, the rheological behavior of the as-prepared hybrid hydrogel was studied using oscillatory rheometry at room temperature (Figure S2). The formation of crosslinking network can be confirmed by the higher storage modulus G' [34], which is eight times larger than the loss modulus G'' at the angular frequency of 10 rad/s. Finally, MSHA was prepared through freeze-drying process.

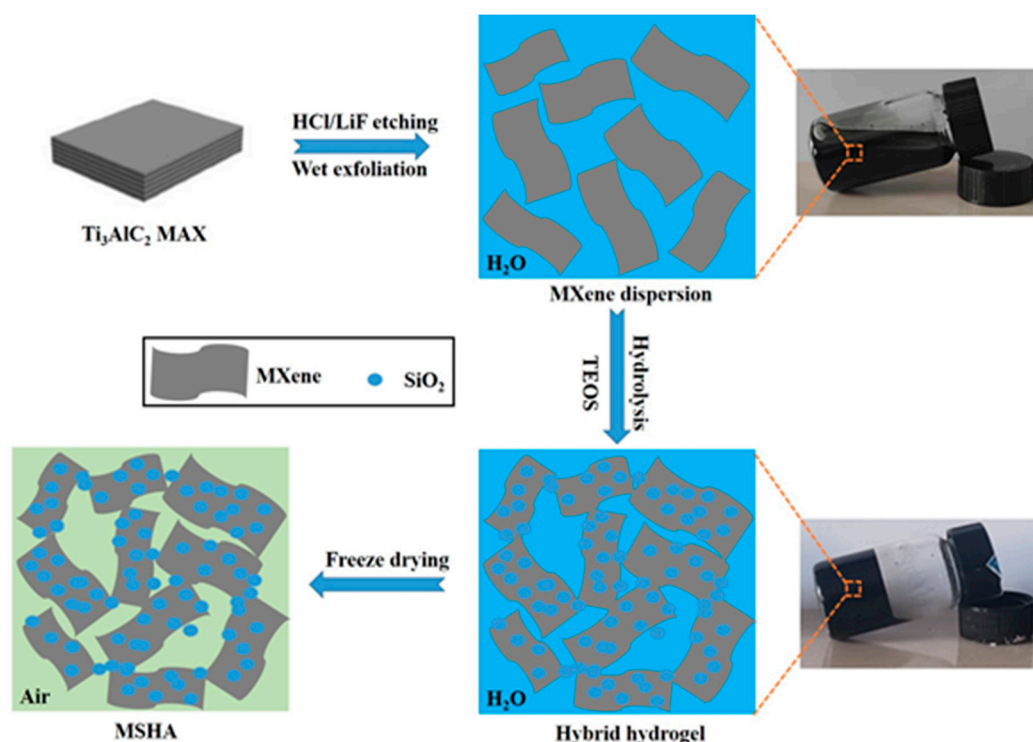


Figure 1. The preparation diagram of MSHA.

2.2. Microstructures of MSHA and $\text{Ti}_3\text{C}_2\text{T}_x$ MXene

The morphology of MSHA and $\text{Ti}_3\text{C}_2\text{T}_x$ MXene samples was analyzed by scanning electron microscope (SEM). $\text{Ti}_3\text{C}_2\text{T}_x$ MXene (Figure 2a) presents a dense plane structure, indicating that MXene sheets are easy to stack closely together. After the hydrolysis and polymerization of TEOS on the MXene surface, the as-prepared MSHA (Figure 2b–d) displays a crumbled 3D porous network. Furthermore, uniform Ti, O, Si, and C elemental distribution images (Figure S3) were observed from the energy-dispersive spectroscopy mapping. The SiO_2 particles should be randomly mixed with MXene.

The phase transition of raw Ti_3AlC_2 , $\text{Ti}_3\text{C}_2\text{T}_x$, SiO_2 , and MSHA was studied by X-ray diffractometer (Figure 2d). The structural evolution of $\text{Ti}_3\text{C}_2\text{T}_x$ and Ti_3AlC_2 was revealed by comparing their X-ray diffraction (XRD) data. The XRD pattern data of Ti_3AlC_2 presents diffraction peaks at $2\theta = 9.5^\circ$, 19.1° , 34.0° , 38.9° , and 41.7° , which can be ascribed to the contribution from (002), (004), (101), (104), and (105) crystal planes. The strongest (104) peak disappears completely due to the LiF/HCl etching treatment. At the same time, the (002) basal plane peak shifts from 9.5° (Ti_3AlC_2) to 6.9° ($\text{Ti}_3\text{C}_2\text{T}_x$ MXene), which is consistent with the reported literature [35,36]. The movement of (002) peak to a relatively lower angle suggests an increase in the spacing of layers. This is due to the removal of element Al in

Ti_3AlC_2 and the introduction of surface termination functional groups ($-\text{F}$, $-\text{O}$, and $-\text{OH}$) in $\text{Ti}_3\text{C}_2\text{T}_x$. For MSHA sample, the peak at 6.9° attributed to the (002) plane of MXene is less pronounced, whereas a new wide peak located at around 23° appears, indicating the successful introduction of amorphous SiO_2 .

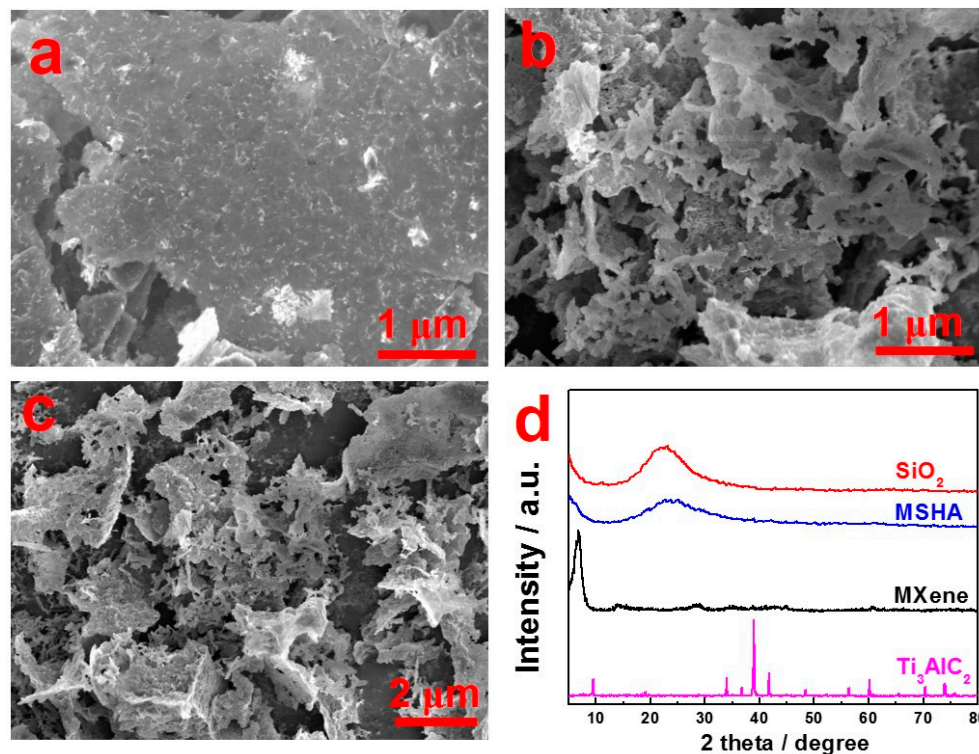


Figure 2. SEM images of the etched $\text{Ti}_3\text{C}_2\text{T}_x$ sample (a) and porous MSHA (b,c); (d) XRD patterns of Ti_3AlC_2 , SiO_2 , MSHA, and $\text{Ti}_3\text{C}_2\text{T}_x$.

X-ray photoelectron spectroscopy (XPS) characterization has been carried out to elucidate the chemical elements and their chemical states. Figure 3a indicates that MXene possesses C, O, F, and Ti elements. There is an additional Si element for MSHA after the introduction of SiO_2 . The Si 2p spectrum (Figure 3b) of MSHA is composed of a SiO_2 peak (103.4 eV), giving evidence to the existence of SiO_2 [37]. As shown in Figure 3c, the C 1s spectra has been divided into four chemical states, including C–Ti (281.8 and 282.9 eV), graphitic C–C (284.7 eV), C–O (286.2 eV), and C=O (288.4 eV), respectively. As displayed in Figure 3d, the Ti 2p spectra has been divided into six chemical states, including Ti–C (455.3 eV), Ti 2p_{3/2} signal (456.5 eV), Ti–OH (458.9 eV), Ti^{2+} (461.2 eV), Ti 2p_{1/2} signal (462.5 eV), and Ti–O_x (464.6 eV), respectively. The O 1s XPS spectra of $\text{Ti}_3\text{C}_2\text{T}_x$ MXene and MSHA can be found in Figure S4, and their O 1s peaks possess two peaks located at 529.9 and 531.8 eV, which might be attributed to C–Ti–O_x and Ti–OH signals, respectively. For MSHA, a new peak centered at 532.5 eV appears (Figure S4), which can be indexed to Si–O group of SiO_2 [37].

The textural properties of the as-prepared MSHA and MXene were illustrated by N_2 sorption analysis. The N_2 sorption isotherm (Figure 4a) of MSHA shows a type-IV isotherm along with a type-H3 hysteresis loop at the high pressure range, indicating the presence of mesopores and macropores. The volume adsorbed at low-pressure range increases sharply, suggesting the existence of micropores [38]. Therefore, the as-prepared hybrid aerogel possesses a hierarchically porous structure. The surface area and pore volume values of the obtained MSHA are $572 \text{ m}^2 \text{ g}^{-1}$ and $1.0 \text{ cm}^3 \text{ g}^{-1}$, respectively, which are larger than those of $\text{Ti}_3\text{C}_2\text{T}_x$ MXene ($13 \text{ m}^2 \text{ g}^{-1}$ and $0.013 \text{ cm}^3 \text{ g}^{-1}$), indicating that the porosity properties were largely enhanced after the introduction of SiO_2 . As displayed in Figure 4b, MSHA shows a wide pore size distribution in the size range of 1–30 nm, while $\text{Ti}_3\text{C}_2\text{T}_x$ lacks these pores due

to the severe stacking of MXene sheets. The micro–meso–macro porous structure of MSHA might be conducive to improving the utilization of sulfur-based cathodes. Furthermore, the porous architecture with adsorption site is also conducive to preventing the shuttle of polysulfides [39].

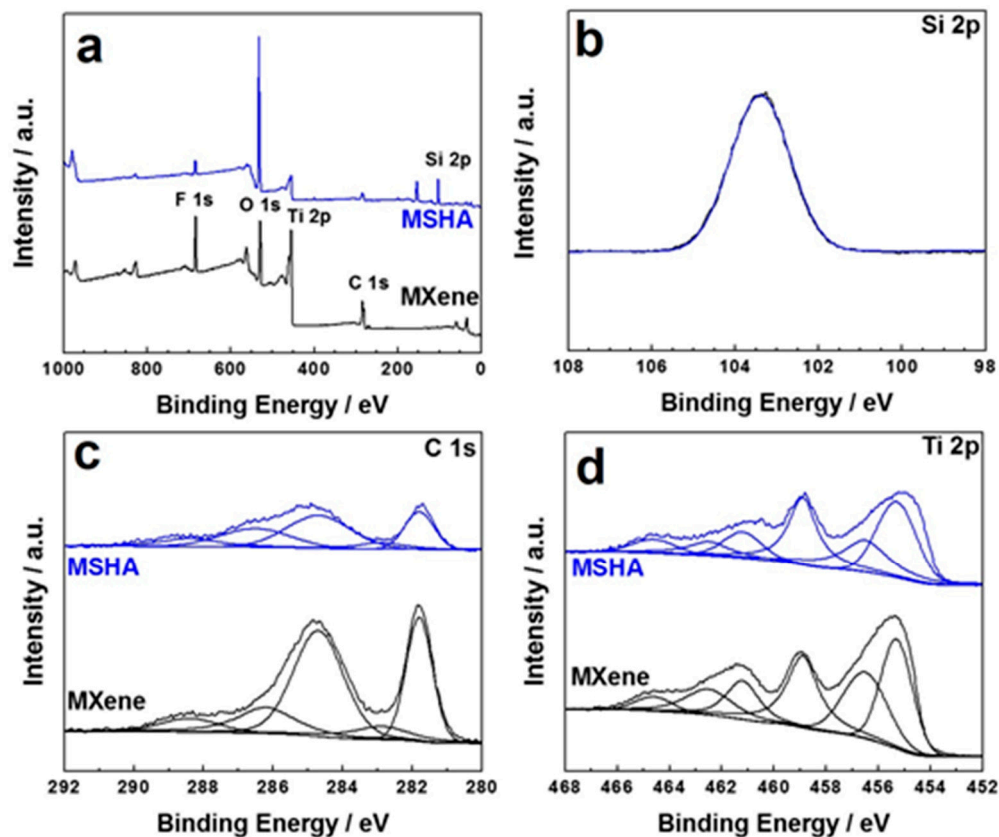


Figure 3. XPS spectra of the as-prepared samples: (a) full survey spectra, (b) Si 2p spectrum of MSHA, (c) C 1s, and (d) Ti 2p spectra.

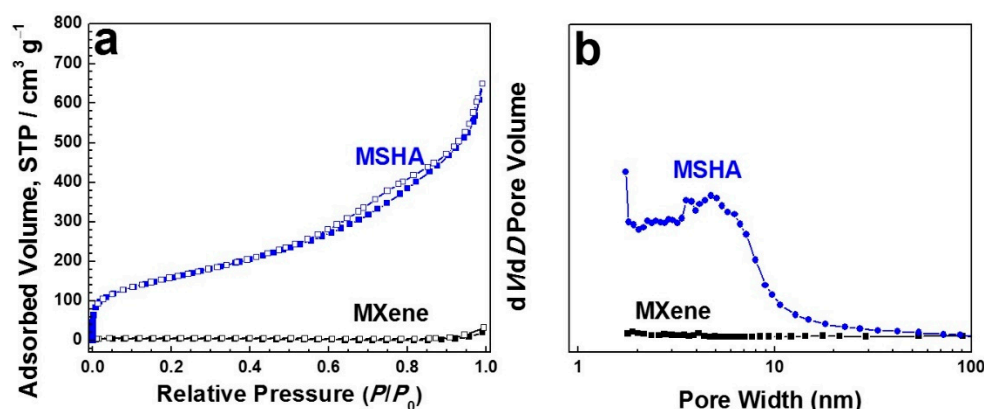


Figure 4. Porous property of the obtained MSHA and MXene: (a) N₂ sorption isotherms and (b) pore size distributions.

2.3. Battery Performance of MSHA as Sulfur Host

MSHA possesses good potential as sulfur host because of its high porosity, stable chemical structure, and polar framework. It has been reported that SiO₂ particles can interact with polysulfides [40]. During charge/discharge process, soluble lithium polysulfides can be formed. Li₂S₆ is one of soluble lithium polysulfides. In our work, the interaction of SiO₂ components and Li₂S₆ was identified by visual observation. As displayed

in Figure 5a, MSHA and MXene were added to Li_2S_6 solution. The color of the solution including MSHA was lighter, compared to MXene, because of the strong adsorption of SiO_2 to polysulfides. Figure 5b presents their corresponding ultraviolet–visible absorption spectra, further confirming the good adsorption capacity of MSHA for Li_2S_6 .

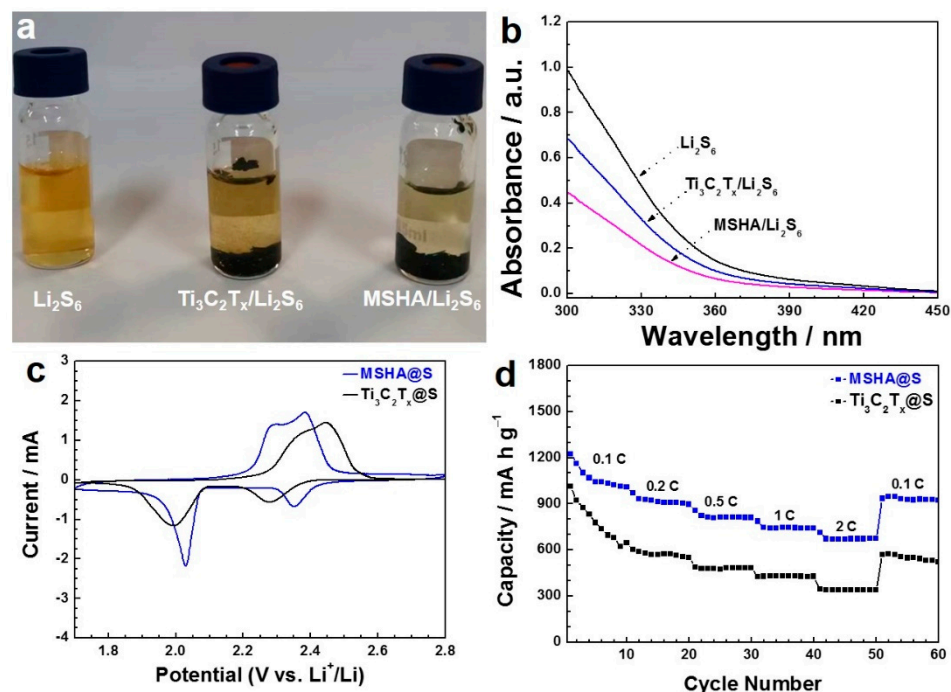


Figure 5. (a) The visual observation on the interaction between the as-prepared samples and polysulfides; (b) the ultraviolet–visible absorption spectra of Li_2S_6 solution in (a); (c) cyclic voltammogram curves of $\text{Ti}_3\text{C}_2\text{T}_x@S$ and $\text{MSHA}@S$ cathodes at 0.1 mV s^{-1} ; (d) rate performance of $\text{MSHA}@S$ and $\text{Ti}_3\text{C}_2\text{T}_x@S$.

In order to evaluate the electrochemical performance of the as-prepared samples as sulfur hosts, $\text{MSHA}@S$ and $\text{Ti}_3\text{C}_2\text{T}_x@S$ were prepared, according to a sulfur impregnation method [41]. A series of electrochemical tests were used to study the electrochemical performance of $\text{MSHA}@S$ (or $\text{Ti}_3\text{C}_2\text{T}_x@S$). The battery was fabricated in a glovebox by employing $\text{MSHA}@S$ (or $\text{Ti}_3\text{C}_2\text{T}_x@S$) as cathode material, metallic lithium as anode, and PP as separator. The cyclic voltammetry was carried out in the potential range of 1.7–2.8 V at 0.1 mV s^{-1} (Figure 5c). There are two strong peaks at about 2.35 and 2.02 V in the cathodic scanning of $\text{MSHA}@S$ cathode. The former can be ascribed to the chemical transition from S_8 to soluble polysulfides (Li_2S_x , $4 \leq x \leq 8$), and the latter is related to the further chemical reduction of high-order polysulfides to low-order Li_2S_2 and Li_2S [42,43]. For the anodic scanning process, there are two peaks at around 2.28 and 2.38 V, which correspond to the chemical reaction of Li_2S to polysulfides, and subsequently to S_8 [44,45].

The charge/discharge experiment was conducted at each current density for ten cycles (Figure 5d), and the corresponding experimental data were shown in Figure S5. $\text{MSHA}@S$ cathode showed a discharge capacity of 1007 mA h g^{-1} (cycle 10) at 0.1 C, 897 mA h g^{-1} (cycle 20) at 0.2 C, and 811 mA h g^{-1} (cycle 30) at 0.5 C, respectively. Even at 1 and 2 C, $\text{MSHA}@S$ still presented discharge capacities of 739 mA h g^{-1} (cycle 40) and 673 mA h g^{-1} (cycle 50), respectively. In particular, a discharge capacity of 923 mA h g^{-1} (cycle 60) was recovered when the current density returned to 0.1 C, suggesting the excellent tolerance and good stability of $\text{MSHA}@S$. Obviously, the reversible discharge capacities of $\text{MSHA}@S$ cathode were higher than those of $\text{Ti}_3\text{C}_2\text{T}_x@S$ cathode. Electrochemical impedance spectroscopy experiments were conducted to acquire more information on $\text{MSHA}@S$ and $\text{Ti}_3\text{C}_2\text{T}_x@S$ cathodes. The data were displayed in Figure 6a. The semicircle at high-frequency region and the inclined line at low-frequency region stand for the charge

transfer resistance and the ion diffusion resistance, respectively [46]. MSHA@S cathode presents a smaller charge transfer resistance than $\text{Ti}_3\text{C}_2\text{T}_x\text{@S}$ cathode, indicating that MSHA could promote electron transport and facilitate ion migration.

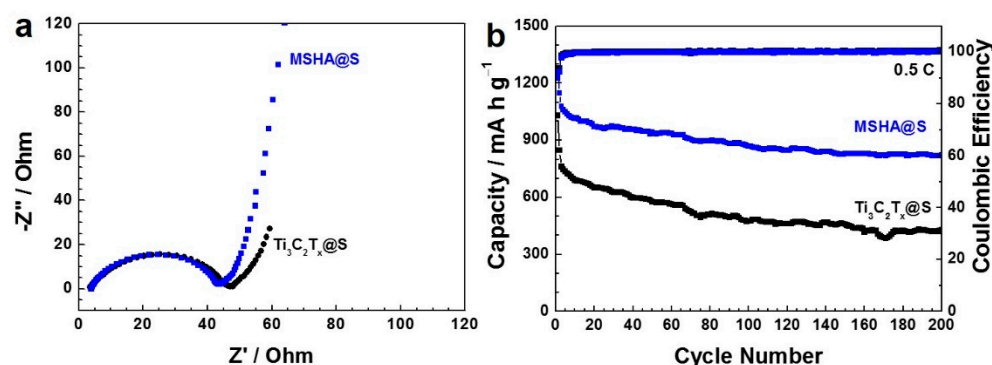


Figure 6. (a) Electrochemical impedance spectroscopy curves and (b) cycling stability (0.5 C) of the batteries with MSHA@S and $\text{Ti}_3\text{C}_2\text{T}_x\text{@S}$ cathodes.

The cycling performance of the battery with MSHA@S cathode was conducted for 200 cycles at 0.5 C (Figure 6b and Figure S6). The assembled battery was activated for two cycles at low current density prior to cycle tests. Apparent from the data, the battery presented an initial specific capacity of 1078 mA h g^{-1} and maintained 823 mA h g^{-1} even after 200 cycles at 0.5 C. However, a low discharge capacity (429 mA h g^{-1}) was observed for the battery with $\text{Ti}_3\text{C}_2\text{T}_x\text{@S}$ cathode. In addition, MSHA@S cathode was superior to many other SiO_2 -based cathodes, such as SiO_2 -coated sulfur particles ($763.2 \text{ mA h g}^{-1}$ at 0.1 C after 50 cycles) and sulfur/ SiO_2 /partially reduced graphene oxide (491 mA h g^{-1} at 0.2 C after 300 cycles) [47,48]. The improved electrochemical properties might be attributed to hierarchically porous network structure and strong interaction between SiO_2 components and polysulfide species. In particular, the synergetic effect of hierarchically micro–meso–macro pore structures plays a vital role: the macroporous structure promotes electrolyte penetration, mesopores provide a way for ion transport and electrolyte diffusion, and the microporous structure serving as a reservoir can inhibit the dissolution of lithium polysulfide species, thus, preventing the shuttle effect [49]. Furthermore, the porous architecture is conducive to buffering volume expansion of sulfur particles during discharge.

2.4. Battery Performance of Modified Separators

Prior to battery performance tests of modified separators, the polysulfide diffusion through the as-prepared separators was studied by H-shaped permeating experiment. It can be observed from Figure S7 that the color of the electrolyte employing PP is darker than that employing MSHA/PP after 32 h, indicating the MSHA/PP separator could alleviate polysulfide shuttle.

Carbon black (CB) was usually applied as a sulfur host to assess the battery performance of modified separator [50]. Therefore, coin cells were assembled based on the S/CB cathode, lithium anode, and the MSHA-functionalized separator. The discharge/charge data of the cell configured with MSHA/PP were shown in Figure S8. There were two charge plateaus and two discharge plateaus in these curves. The discharge plateaus are related to the chemical transition from S_8 to soluble polysulfide species (Li_2S_x , $4 \leq x \leq 8$) and further to Li_2S_2 and Li_2S . The charge plateaus stand for the chemical oxidation of Li_2S to polysulfides and eventually to S_8 [42]. It can be observed from experimental data that the plateaus of the cell with MSHA/PP are obvious at 2.0 C. It could be deduced accordingly that the MSHA/PP might effectively prevent the shuttle of polysulfides. The charge/discharge tests of the cell with MSHA/PP were studied at each current density for ten cycles (Figure 7a). It is obvious that the rate capability of the cell with MSHA/PP was superior to that with PP separator, indicating that the MSHA/PP was more beneficial for rapid electron/ion transport and redox reaction kinetics than PP separator.

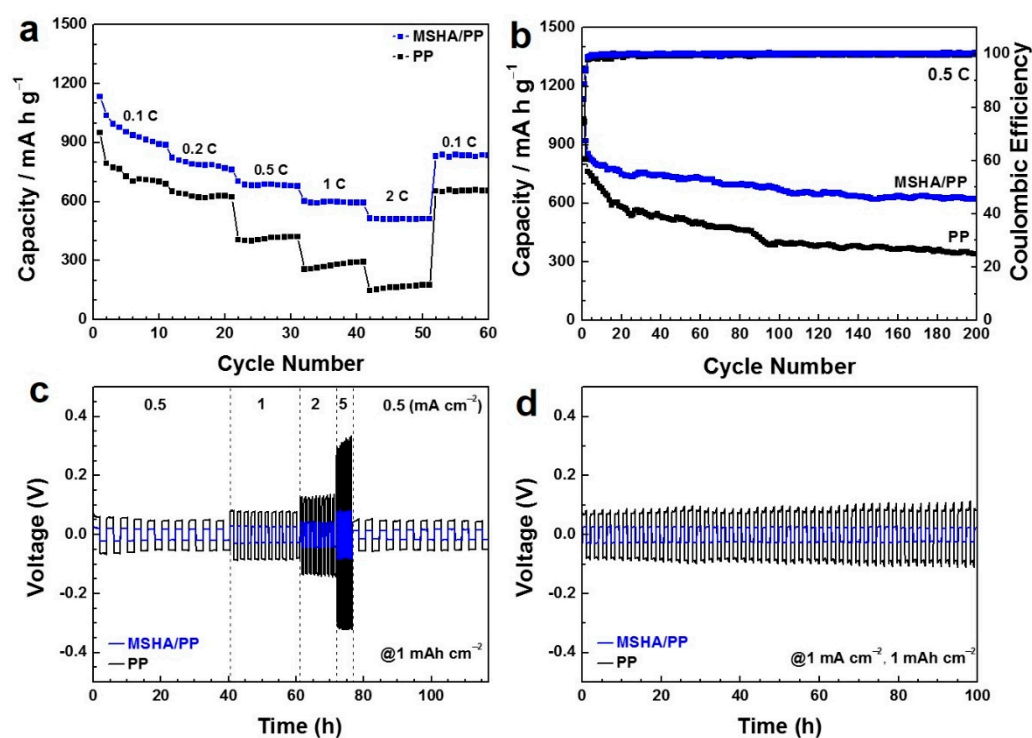


Figure 7. (a) Rate capability and (b) cycling stability of the cells configured with MSHA/PP and PP; (c) rate capability, and (d) cycling performance of Li||Li symmetric cells configured with MSHA/PP and PP.

The cycling performances of the cell with different separators over 200 cycles at 0.5 C were studied (Figure 7b). According to their charge/discharge experimental data (Figure S9), the assembled cell with MSHA/PP also presents two discharge platforms, corresponding to the conversion of S_8 to polysulfides, and subsequently to Li_2S_2/Li_2S . The cell with MSHA/PP delivers a decent discharge capacity of 623 mA h g^{-1} after 200 cycles at 0.5 C. In contrast, the cell with PP separator shows a low capacity and fast decay (from 762 mA h g^{-1} to 340 mA h g^{-1}) during cycling. The above analysis indicates that MSHA/PP plays a vital role in inhibiting polysulfides shuttling and improving redox reaction kinetics. In addition, MSHA/PP separator was also superior to the SiO_2 -based separator previously reported ($603.5 \text{ mA h g}^{-1}$ at 0.2 C after 200 cycles) [30]. The improved electrochemical performance of the cell with MSHA/PP might be attributed to the following reasons. First, the 3D conductive $Ti_3C_2T_x$ -based framework with porous structure is beneficial for the electron/ion accessibility. Second, the rich functional groups in MSHA are conducive to the adsorption of polysulfides, thus, alleviating the shuttle effect [51]. Furthermore, we also studied the effect of MSHA-modified separator on lithium anode by means of the Li||Li symmetric battery method. As shown in Figure 7c, compared with PP, MSHA/PP presents narrower voltage hysteresis. Figure 7d exhibits cycle performance of Li||Li symmetric batteries configured with MSHA/PP and PP. Obviously, the cell with MSHA/PP displays a low polarization behavior, indicative of the effective suppression of dendrite growth [50].

3. Materials and Methods

3.1. Preparation of MXene/ SiO_2 Hybrid Aerogel (MSHA) Material

The preparation process of $Ti_3C_2T_x$ MXene dispersion was provided in the supplementary file. During the preparation of MSHA, TEOS (0.5 mL), ethanol (2 mL), and deionized water (4 mL) were first mixed together. To promote the hydrolysis of TEOS, an appropriate amount of hydrochloric acid was added until the pH value of the mixture became around 4. After stirring at room temperature for 15 min, in order to promote the further condensation of TEOS, an appropriate amount of ammonia was added to the mixture to place its pH

near 8. Subsequently, 6 mL of $\text{Ti}_3\text{C}_2\text{T}_x$ MXene dispersion (10 mg mL^{-1}) was added into the above mixture. Afterwards, the mixture was treated at 35°C for 72 h to form a black hydrogel through a sol-gel method. In the above process, TEOS was simultaneously converted to SiO_2 . MXene/ SiO_2 hybrid aerogel (MSHA) was prepared by purifying the obtained hydrogel with ultrapure water, followed by vacuum freeze-drying of the hybrid hydrogel for 24 h.

3.2. Preparation of MSHA@S Composite

First, 40 mg of the hybrid aerogel material was added to the mortar, and then 60 mg of the sublimated sulfur powder was added. After thoroughly grinding the above mixture for 30 min, it was transferred to a horizontal tubular furnace and further heated for 12 h 155°C . The sample was collected after the tubular furnace was allowed to cool to room temperature. The as-obtained product was marked as MSHA@S. $\text{Ti}_3\text{C}_2\text{T}_x$ @S and S/carbon black (S/CB) composites were synthesized under the same conditions.

3.3. Preparation of MSHA Modified Separator

Typically, 80 wt% of the MSHA, 10 wt% of carbon black, and 10 wt% of polyvinylidene fluoride were mixed together and dispersed in a solvent of N-methyl-2-pyrrolidinone. Then, the obtained slurry was coated onto the Celgard2500 PP separator. MSHA modified PP separator (MSHA/PP) can be prepared after drying it at 60°C overnight.

3.4. Material Characterization and Electrochemical Measurement

The information on material characterization and electrochemical measurement can be found in the supplementary file.

4. Conclusions

In summary, we report a unique porous material, namely, MSHA with a high specific surface area ($572 \text{ m}^2 \text{ g}^{-1}$) via facile sol-gel and freeze-drying methods. The as-prepared porous material displays a 3D interconnected network structure assembled by $\text{Ti}_3\text{C}_2\text{T}_x$ MXene and SiO_2 . The hierarchically porous MSHA can be used not only as a new sulfur host to prepare sulfur-based cathode material but also as an efficient functional separator to alleviate the shuttle effect of polysulfides. MSHA as a sulfur carrier exhibits excellent electrochemical performance with a high-rate capability of 673 mA h g^{-1} at 2 C and a good cycling performance of 823 mA h g^{-1} after 200 cycles at 0.5 C. Furthermore, the battery assembled with MSHA-modified separator shows high capacities of 623 mA h g^{-1} after 200 cycles at 0.5 C. This work may promote the development of MXene-based aerogels for high-performance Li-S battery.

Supplementary Materials: The following supporting information can be downloaded at: <https://www.mdpi.com/article/10.3390/molecules27207073/s1>, Figure S1: Transmission electron microscopy picture of $\text{Ti}_3\text{C}_2\text{T}_x$ MXene nanosheets; Figure S2: The rheological behavior of the as-prepared hybrid hydrogel; Figure S3: The SEM image of porous MSHA and its corresponding elemental mapping; Figure S4: O 1s XPS spectra of MSHA and $\text{Ti}_3\text{C}_2\text{T}_x$ MXene; Figure S5: Charge/discharge curves of the cell with the MSHA@S cathode from 0.1 to 2.0 C; Figure S6: Charge/discharge curves of the cell with the MSHA@S cathode at 0.5 C; Figure S7: Visualization of the polysulfide diffusion across MSHA/PP and PP separators; Figure S8: Charge/discharge curves of the cell with MSHA/PP separator from 0.1 to 2.0 C; Figure S9: Charge/discharge curves of the cell with MSHA/PP separator at 0.5 C. Reference [31] is cited in the supplementary materials.

Author Contributions: Conceptualization, J.Z., Z.S. and Q.C.; methodology, J.Q., J.Z. and Q.C.; validation, J.Z., Z.P. and Y.L. (Ying Liang); formal analysis, J.Q. and Y.L. (Yongpeng Li); investigation, J.Z. and X.X.; data curation, J.Z., Z.S. and Y.L. (Yulin Li); writing—original draft preparation, J.Z., Z.P. and Y.L. (Ying Liang); writing—review and editing, J.Z., Z.S. and Q.C.; visualization, J.Z.; supervision, J.Q., Z.S. and Q.C. All authors have read and agreed to the published version of the manuscript.

Funding: This research was funded by the National Natural Science Foundation of China (Grant Nos. 21975058, 52063014, and 22101244), Hainan Province Science and Technology Special Fund (ZDYF2022SHFZ299), Youth Innovation Technology Project of Higher School in Shandong Province (2020KJC002), and Taishan Scholar Project of Shandong Province (tsqn201909087).

Institutional Review Board Statement: Not applicable.

Informed Consent Statement: Not applicable.

Data Availability Statement: Not applicable.

Conflicts of Interest: The authors declare no conflict of interest.

References

1. Lin, L.; Lei, W.; Zhang, S.; Liu, Y.; Wallace, G.G.; Chen, J. Two-dimensional transition metal dichalcogenides in supercapacitors and secondary batteries. *Energy Storage Mater.* **2019**, *19*, 408–423. [[CrossRef](#)]
2. Zhang, W.; Li, S.; Zhou, A.; Song, H.; Cui, Z.; Du, L. Recent advances and perspectives in lithium–sulfur pouch cells. *Molecules* **2021**, *26*, 6341. [[CrossRef](#)]
3. Sehk, Z.W.; Sun, Y.; Zhang, Q.; Cui, Y. Designing high-energy lithium-sulfur batteries. *Chem. Soc. Rev.* **2016**, *45*, 5605–5634.
4. Zhang, Y.; Liu, Y.; Zhao, Z.; Guo, Y.; Li, Q.; Liu, P.; Hu, B.; Wang, L.; Lu, H. Horizontally aligned lamellar porous graphene/nickel composite for high volumetric capacity lithium-sulfur batteries. *Appl. Surf. Sci.* **2022**, *586*, 152805. [[CrossRef](#)]
5. Zhang, N.; Li, B.; Li, S.; Yang, S. Mesoporous hybrid electrolyte for simultaneously inhibiting lithium dendrites and polysulfide shuttle in Li–S batteries. *Adv. Energy Mater.* **2018**, *8*, 1703124. [[CrossRef](#)]
6. Peng, H.-J.; Zhang, G.; Chen, X.; Zhang, Z.-W.; Xu, W.-T.; Huang, J.-Q.; Zhang, Q. Enhanced electrochemical kinetics on conductive polar mediators for lithium–sulfur batteries. *Angew. Chem. Int. Ed.* **2016**, *55*, 12990–12995. [[CrossRef](#)]
7. Yang, T.; Xia, J.; Piao, Z.; Yang, L.; Zhang, S.; Xing, Y.; Zhou, G. Graphene-based materials for flexible lithium–sulfur batteries. *ACS Nano* **2021**, *15*, 13901–13923. [[CrossRef](#)]
8. Tian, J.; Xing, F.; Gao, Q. Graphene-based nanomaterials as the cathode for lithium-sulfur batteries. *Molecules* **2021**, *26*, 2507. [[CrossRef](#)] [[PubMed](#)]
9. Yang, W.; Yang, W.; Feng, J.; Qin, X. A polypyrrole-coated acetylene black/sulfur composite cathode material for lithium–sulfur batteries. *J. Energy Chem.* **2018**, *27*, 813–819. [[CrossRef](#)]
10. Zhou, X.; Chen, F.; Yang, J. Core@shell sulfur@polypyrrole nanoparticles sandwiched in graphene sheets as cathode for lithium-sulfur batteries. *J. Energy Chem.* **2015**, *24*, 448–455. [[CrossRef](#)]
11. Wang, J.; Yang, Y.; Kang, F. Porous carbon nanofiber paper as an effective interlayer for high-performance lithium-sulfur batteries. *Electrochim. Acta* **2015**, *168*, 271–276. [[CrossRef](#)]
12. Zhu, Y.; Xu, G.; Zhang, X.; Wang, S.; Li, C.; Wang, G. Hierarchical porous carbon derived from soybean hulls as a cathode matrix for lithium-sulfur batteries. *J. Alloys Compd.* **2022**, *906*, 164341. [[CrossRef](#)]
13. Fang, R.; Chen, K.; Yin, L.; Sun, Z.; Li, F.; Cheng, H.-M. The regulating role of carbon nanotubes and graphene in lithium-ion and lithium-sulfur batteries. *Adv. Mater.* **2019**, *31*, 1800863. [[CrossRef](#)]
14. Seh, Z.W.; Li, W.; Cha, J.J.; Zheng, G.; Yang, Y.; McDowell, M.T.; Hsu, P.-C.; Cui, Y. Sulphur-TiO₂ yolk-shell nanoarchitecture with internal void space for long-cycle lithium-sulphur batteries. *Nat. Commun.* **2013**, *4*, 1331. [[CrossRef](#)]
15. Dong, W.; Meng, L.; Hong, X.; Liu, S.; Shen, D.; Xia, Y.; Yang, S. MnO₂/rGO/CNTs framework as a sulfur host for high-performance Li-S batteries. *Molecules* **2020**, *25*, 1989. [[CrossRef](#)]
16. Lee, S.-K.; Kim, H.; Bang, S.; Myung, S.-T.; Sun, Y.-K. WO₃ nanowire/carbon nanotube interlayer as a chemical adsorption mediator for high-performance lithium-sulfur batteries. *Molecules* **2021**, *26*, 377. [[CrossRef](#)] [[PubMed](#)]
17. Huang, Y.-C.; Yen, Y.-J.; Tseng, Y.-H.; Chung, S.-H. Module-designed carbon-coated separators for high-loading, high-sulfur-utilization cathodes in lithium–sulfur batteries. *Molecules* **2022**, *27*, 228. [[CrossRef](#)]
18. Wang, H.; Zhang, W.; Liu, H.; Guo, Z. A strategy for configuration of an integrated flexible sulfur cathode for high-performance lithium-sulfur batteries. *Angew. Chem. Int. Ed.* **2016**, *55*, 3992–3996. [[CrossRef](#)]
19. Wu, P.; Tan, L.; Wang, X.-D.; Liao, P.; Liu, Z.; Hou, P.-P.; Zhou, Q.-Y.; Jin, X.-J.; Li, M.-C.; Shao, X.-R.; et al. Porous 3D nitrogen-doped rGO/Co-Ni-S composite modified separator for high-capacity and stable lithium-sulfur batteries. *Mater. Res. Bull.* **2022**, *145*, 111550. [[CrossRef](#)]
20. Balach, J.; Singh, H.K.; Gomoll, S.; Jaumann, T.; Klose, M.; Oswald, S.; Richter, M.; Eckert, J.; Giebeler, L. Synergistically enhanced polysulfide chemisorption using a flexible hybrid separator with N and S dual-doped mesoporous carbon coating for advanced lithium–sulfur batteries. *ACS Appl. Mater. Interfaces* **2016**, *8*, 14586–14595. [[CrossRef](#)]
21. Xu, G.; Yan, Q.B.; Wang, S.; Kushima, A.; Bai, P.; Liu, K.; Zhang, X.; Tang, Z.; Li, J. A thin multifunctional coating on a separator improves the cyclability and safety of lithium sulfur batteries. *Chem. Sci.* **2017**, *8*, 6619–6625. [[CrossRef](#)] [[PubMed](#)]
22. Bai, S.; Liu, X.; Zhu, K.; Wu, S.; Zhou, H. Metal–organic framework-based separator for lithium–sulfur batteries. *Nat. Energy* **2016**, *1*, 16094. [[CrossRef](#)]
23. Huang, J.-Q.; Zhuang, T.-Z.; Zhang, Q.; Peng, H.-J.; Chen, C.-M.; Wei, F. Permselective graphene oxide membrane for highly stable and anti-self-discharge lithium–sulfur batteries. *ACS Nano* **2015**, *9*, 3002–3011. [[CrossRef](#)] [[PubMed](#)]

24. Sun, J.; Sun, Y.; Pasta, M.; Zhou, G.; Li, Y.; Liu, W.; Xiong, F.; Cui, Y. Entrapment of polysulfides by a black-phosphorus-modified separator for lithium-sulfur batteries. *Adv. Mater.* **2016**, *28*, 9797–9803. [[CrossRef](#)] [[PubMed](#)]
25. Xie, X.; Zhao, M.; Anasori, B.; Maleski, K.; Ren, C.E.; Li, J.; Byles, B.W.; Pomerantseva, E.; Wang, G.; Gogotsi, Y. Porous heterostructured MXene/carbon nanotube composite paper with high volumetric capacity for sodium-based energy storage devices. *Nano Energy* **2016**, *26*, 513–523. [[CrossRef](#)]
26. Anasori, B.; Lukatskaya, M.R.; Gogotsi, Y. 2D metal carbides and nitrides (MXenes) for energy storage. *Nat. Rev. Mater.* **2017**, *2*, 16098. [[CrossRef](#)]
27. Tang, H.; Li, W.; Pan, L.; Tu, K.; Du, F.; Qiu, T.; Yang, J.; Cullen, C.P.; McEvoy, N.; Zhang, C. A robust, freestanding MXene-sulfur conductive paper for long-lifetime Li-S batteries. *Adv. Funct. Mater.* **2019**, *29*, 1901907. [[CrossRef](#)]
28. Xiong, C.; Zhu, G.Y.; Jiang, H.R.; Chen, Q.; Zhao, T.S. Achieving multiplexed functionality in a hierarchical MXene-based sulfur host for high-rate, high-loading lithium-sulfur batteries. *Energy Storage Mater.* **2020**, *33*, 147–157. [[CrossRef](#)]
29. Kou, W.; Li, X.; Liu, Y.; Zhang, X.; Yang, S.; Jiang, X.; He, G.; Dai, Y.; Zheng, W.; Yu, G. Triple-layered carbon-SiO₂ composite membrane for high energy density and long cycling Li–S batteries. *ACS Nano* **2019**, *13*, 5900–5909. [[CrossRef](#)]
30. Li, J.; Huang, Y.; Zhang, S.; Jia, W.; Wang, X.; Guo, Y.; Jia, D.; Wang, L. Decoration of silica nanoparticles on polypropylene separator for lithium-sulfur batteries. *ACS Appl. Mater. Interfaces* **2017**, *9*, 7499–7504. [[CrossRef](#)]
31. Lin, L.-W.; Qi, M.; Bai, Z.-T.; Yan, S.-X.; Sui, Z.-Y.; Han, B.-H.; Liu, Y.-W. Crumpled nitrogen-doped aerogels derived from MXene and pyrrole-formaldehyde as modified separators for stable lithium-sulfur batteries. *Appl. Surf. Sci.* **2021**, *555*, 149717. [[CrossRef](#)]
32. Jiang, Y.; Xie, X.; Chen, Y.; Liu, Y.; Yang, R.; Sui, G. Hierarchically structured cellulose aerogels with interconnected MXene networks and their enhanced microwave absorption properties. *J. Mater. Chem. C* **2018**, *6*, 8679–8687. [[CrossRef](#)]
33. Hui, X.; Zhao, R.; Zhang, P.; Li, C.; Wang, C.; Yin, L. Low-temperature reduction strategy synthesized Si/Ti₃C₂ MXene composite anodes for high-performance Li-ion batteries. *Adv. Energy Mater.* **2019**, *9*, 1901065. [[CrossRef](#)]
34. Sui, Z.; Zhang, X.; Lei, Y.; Luo, Y. Easy and green synthesis of reduced graphite oxide-based hydrogels. *Carbon* **2011**, *49*, 4314–4321. [[CrossRef](#)]
35. Zhang, T.; Pan, L.; Tang, H.; Du, F.; Guo, Y.; Qiu, T.; Yang, J. Synthesis of two-dimensional Ti₃C₂T_x MXene using HCl plus LiF etchant: Enhanced exfoliation and delamination. *J. Alloys Compd.* **2017**, *695*, 818–826. [[CrossRef](#)]
36. Ma, J.; Cheng, Y.; Wang, L.; Dai, X.; Yu, F. Free-standing Ti₃C₂T_x MXene film as binder-free electrode in capacitive deionization with an ultrahigh desalination capacity. *Chem. Eng. J.* **2020**, *384*, 123329. [[CrossRef](#)]
37. Mu, G.; Mu, D.; Wu, B.; Ma, C.; Bi, J.; Zhang, L.; Yang, H.; Wu, F. Microsphere-like SiO₂/MXene hybrid material enabling high performance anode for lithium ion batteries. *Small* **2020**, *16*, 1905430. [[CrossRef](#)]
38. Zeng, F.; Sui, Z.; Liu, S.; Liang, H.; Zhan, H.; Han, B. Nitrogen-doped carbon aerogels with high surface area for supercapacitors and gas adsorption. *Mater. Today Commun.* **2018**, *16*, 1–7. [[CrossRef](#)]
39. Bao, W.; Liu, L.; Wang, C.; Choi, S.; Wang, D.; Wang, G. Facile synthesis of crumpled nitrogen-doped MXene nanosheets as a new sulfur host for lithium-sulfur batteries. *Adv. Energy Mater.* **2018**, *8*, 1702485. [[CrossRef](#)]
40. Xue, W.; Yan, Q.-B.; Xu, G.; Suo, L.; Chen, Y.; Wang, C.; Wang, C.-A.; Li, J. Double-oxide sulfur host for advanced lithium-sulfur batteries. *Nano Energy* **2017**, *38*, 12–18. [[CrossRef](#)]
41. Liang, Y.; Xia, T.; Chang, Z.; Xie, W.; Li, Y.; Li, C.; Fan, R.; Wang, W.; Sui, Z.; Chen, Q. Boric acid functionalized triazine-based covalent organic frameworks with dual-function for selective adsorption and lithium-sulfur battery cathode. *Chem. Eng. J.* **2022**, *437*, 135314. [[CrossRef](#)]
42. Liu, X.; Xia, M.; Zhao, Y.; Xia, T.; Li, Y.; Xiao, J.; Sui, Z.; Chen, Q. Cationic covalent organic framework via cycloaddition reactions as sulfur-loaded matrix for lithium-sulfur batteries. *Mater. Today Chem.* **2022**, *23*, 100664.
43. Liang, Y.; Xia, M.; Zhao, Y.; Wang, D.; Li, Y.; Sui, Z.; Xiao, J.; Chen, Q. Functionalized triazine-based covalent organic frameworks containing quinoline via aza-Diels-Alder reaction for enhanced lithium-sulfur batteries performance. *J. Colloid Interf. Sci.* **2022**, *608*, 652–661. [[CrossRef](#)] [[PubMed](#)]
44. Zhou, H.-Y.; Sui, Z.-Y.; Zhao, F.-L.; Sun, Y.-N.; Wang, H.-Y.; Han, B.-H. A nanostructured porous carbon/MoO₂ composite with efficient catalysis in polysulfide conversion for lithium-sulfur batteries. *Nanotechnology* **2020**, *31*, 315601. [[CrossRef](#)] [[PubMed](#)]
45. Zhou, H.-Y.; Sui, Z.-Y.; Amin, K.; Lin, L.-W.; Wang, H.-Y.; Han, B.-H. Investigating the electrocatalysis of a Ti₃C₂/carbon hybrid in polysulfide conversion of lithium-sulfur batteries. *ACS Appl. Mater. Interfaces* **2020**, *12*, 13904–13913. [[CrossRef](#)]
46. Abbas, S.A.; Ibrahim, M.A.; Hu, L.H.; Lin, C.N.; Fang, J.; Boopathi, K.M.; Wang, P.; Li, L.J.; Chu, C.W. Bifunctional separator as a polysulfide mediator for highly stable Li-S batteries. *J. Mater. Chem. A* **2016**, *4*, 9661–9669. [[CrossRef](#)]
47. Campbell, B.; Bell, J.; Bay, H.; Favors, Z.; Ionescu, R.; Ozkan, C.S.; Ozkan, M. SiO₂-coated sulfur particles with mildly reduced graphene oxide as a cathode material for lithium-sulfur batteries. *Nanoscale* **2015**, *7*, 7051–7055. [[CrossRef](#)]
48. Rajkumar, P.; Diwakar, K.; Subadevi, R.; Gnanamuthu, R.M.; Wang, F.; Liu, W.; Sivakumar, M. Graphene sheet-encased silica/sulfur composite cathode for improved cyclability of lithium-sulfur batteries. *J. Solid State Electr.* **2021**, *25*, 939–948. [[CrossRef](#)]
49. Wu, H.; Tang, Q.; Fan, H.; Liu, Z.; Hu, A.; Zhang, S.; Deng, W.; Chen, X. Dual-confined and hierarchical-porous graphene/C/SiO₂ hollow microspheres through spray drying approach for lithium-sulfur batteries. *Electrochim. Acta* **2017**, *255*, 179–186. [[CrossRef](#)]

-
50. Xu, J.; An, S.; Song, X.; Cao, Y.; Wang, N.; Qiu, X.; Zhang, Y.; Chen, J.; Duan, X.; Huang, J.; et al. Towards high performance Li-S batteries via sulfonate-rich COF-modified separator. *Adv. Mater.* **2021**, *33*, 2105178. [[CrossRef](#)]
 51. Yin, L.; Xu, G.; Nie, P.; Dou, H.; Zhang, X. MXene debris modified eggshell membrane as separator for high-performance lithium-sulfur batteries. *Chem. Eng. J.* **2018**, *352*, 695–703. [[CrossRef](#)]